Communication

Microstructural Evolution of Shear Localization in High-Speed Cutting of CoCrFeMnNi High-Entropy Alloy

Ming-Yao Su [1,2], Wei-Han Zhang [1,2], Yuan-Yuan Tan [1], Yan Chen [1,2,*], Hai-Ying Wang [1,2] and Lan-Hong Dai [1,2,*]

1   State Key Laboratory of Nonlinear Mechanics, Institute of Mechanics, Chinese Academy of Sciences,
    Beijing 100190, China; sumingyao@imech.ac.cn (M.-Y.S.); zhangweihan22@mails.ucas.ac.cn (W.-H.Z.);
    yuanyuantan@lnm.imech.ac.cn (Y.-Y.T.); why@lnm.imech.ac.cn (H.-Y.W.)
2   School of Engineering Science, University of Chinese Academy of Sciences, Beijing 101408, China
*   Correspondence: chenyan@lnm.imech.ac.cn (Y.C.); lhdai@lnm.imech.ac.cn (L.-H.D.)

Abstract: Shear localization is one of the most important failure mechanisms subjected to high-strain-rate deformation and has significant effects on the process, plastic deformation, and catastrophic failure of a material. Shear localization was observed in serrated chips produced during the high-speed cutting of the CoCrFeMnNi high-entropy alloy. Electron backscatter diffraction was performed to systematically investigate microstructural evolution during shear banding. The elongation and subdivision of the narrow grains were observed in the areas adjacent to the shear band. The microstructure inside the shear band was found to be composed of equiaxed ultrafine grains. The results reveal that grain subdivision and dynamic recrystallization might have significant roles in the microstructural evolution of shear bands. These results offer key insights into our understanding of shear localization and high-speed machining behavior for high entropy alloys.

Keywords: high-entropy alloy; high-speed cutting; shear bands; dynamic recrystallization

1. Introduction

High speed cutting is a promising advanced manufacturing technique and has been widely used in the aerospace, die and mold fabrication, and automotive industries [1,2]. During the cutting process, a workpiece material is transformed into chips after undergoing severe plastic deformation. The role of chips is of central importance, because chips are witnesses to the whole physical and thermal phenomenon [3]. The emergence of serrated chip flow is a universal phenomenon during the high-speed cutting process [4–7]. Therefore, understanding the mechanism of serrated chip flow is critical for the development of high-speed machining techniques. During the past few decades, lots of studies have shown that these serrated chips are attributed to repeated thermoplastic shear banding instability which occurs within the primary shear zone (PSZ) [8–13]. The shear band is one of the most important failure mechanisms subjected to high-strain-rate deformation and is generally considered as the precursor to the catastrophic failure of a material [14–18]. It is noted that shear localization behavior during high-speed cutting is not only related to cutting conditions but is also sensitive to the workpiece material.

High-entropy alloys (HEAs) or complex concentrated alloys are a relatively interesting class of metal materials that contain multiple elements in equiatomic and near-equiatomic ratios. Due to their unique chemical complexity caused by the random distribution of elements in the lattice, HEAs display superior properties, including remarkable fracture toughness [19–21], an outstanding combination of strength and ductility [22–24], excellent resistance to hydrogen embrittlement [25,26], good damage tolerance [27–29], and exceptional dynamic mechanical performance [30–32]. Therefore, they have wide potential application prospects, such as aerospace, nuclear reactor, kinetic energy penetrators, and other engineering applications [33,34]. However, to date, the nature of the deformation

behavior of HEAs during high-speed cutting remains unclear. Hence, understanding of the shear localization of HEAs in high-speed cutting is needed.

In this paper, we reported the design and results of high-speed cutting experiments for the CoCrFeMnNi high-entropy alloy for the first time. The microstructure evolution of shear localization in the obtained chips was investigated using electron backscatter diffraction (EBSD). The heterogeneous deformation gradient distribution in the chips leads to the formation of elongation grains in the areas adjacent to the shear band and equiaxed ultrafine grains in the core of shear band. Furthermore, a microstructure evolution model was proposed. The results advance our understanding of shear banding and high-speed machining behavior for high-entropy alloys.

2. Materials and Methods

The equiatomic $Co_{20}Cr_{20}Fe_{20}Mn_{20}Ni_{20}$ (at%) HEA was synthesized by arc-melting high purity elements (at least 99.9% purity) under an argon atmosphere. The ingots were remelted at least five times to improve their chemical homogeneity. The as-cast ingots were cold rolled by a 45% reduction in thickness and subsequently annealed at 1073 K for 1 h in vacuum to eliminate the residual stress and fully recrystallize. The as-annealed sheets were cut into rectangular workpieces with dimensions of 40 mm × 40 mm × 2 mm via electric discharge machining.

High-speed cutting tests were conducted on a self-developed experimental device based on split Hopkinson pressure bar (SHPB) [35], schematically shown in Figure 1. In these sets of tests, uncoated tools made of P10 tungsten carbide material were designed with rake angles of 0° and clearance angles of 5°. The principal machining parameters were used in the orthogonal cutting for the cutting speed of 15 m/s and a constant cutting thickness of 200 μm. The serrated chips were collected for each experiment, mounted, and polished for further metallographic examinations. Microstructural characterizations were carried out on a field emission scanning electron microscope (SEM, JSM-7900F, JEOL Inc., Tokyo, Japan) equipped with electron backscatter diffraction (EBSD, EDAX Hikari Super, AMETEK Inc., Mahwah, NJ, USA) before and after high speed cutting. In the EBSD data analysis, the low-angle grain boundaries (LAGBs) with misorientations of 2–15° and the high-angle grain boundaries (HAGBs) with misorientations of above 15° were indicated with white and black lines, respectively.
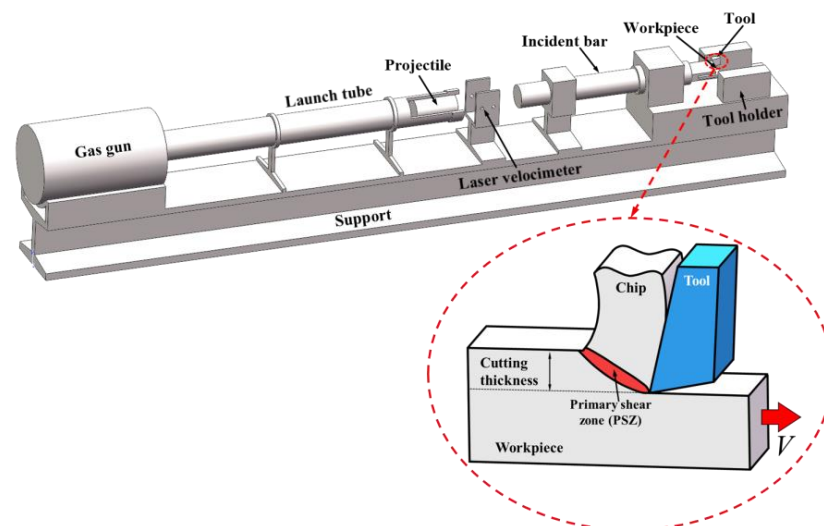

Figure 1. Diagram of high-speed cutting experimental device based on a split Hopkinson pressure bar (SHPB). The insert shows the schematic diagram of the cutting process.

3. Results and Discussion

The initial workpiece had equiaxed grains with a mean grain size of 32 μm, as shown in the EBSD in Figure 2a. Annealing twins were formed in the grain interior. In addition,

the EBSD inverse pole figure (IPF) orientation map indicated that the equiaxed grains were randomly orientated (Figure 2b). With regard to the chip after high-speed cutting, Figure 3 shows the serrated chip morphology from SEM and the characteristics of the shear band from EBSD. From Figure 3b, the shear bands with highly localized deformation were observed between the saw-teeth-like chips. The propagated direction of the band was the maximum shear deformation direction. In the bulk of the segment, grains adjacent to the shear band were deformed and elongated toward the shear direction. It was evident that the shear deformation away from the shear band was relatively low, since the microstructures of grains within this region basically kept their original features. It is important to note that the information regarding the grains indicated the severe deformation gradient in the direction perpendicular to the shear band from near to far away, as shown in Figure 3b. This methodology has been exploited as a means for investigating the microstructure evolution of shear bands.
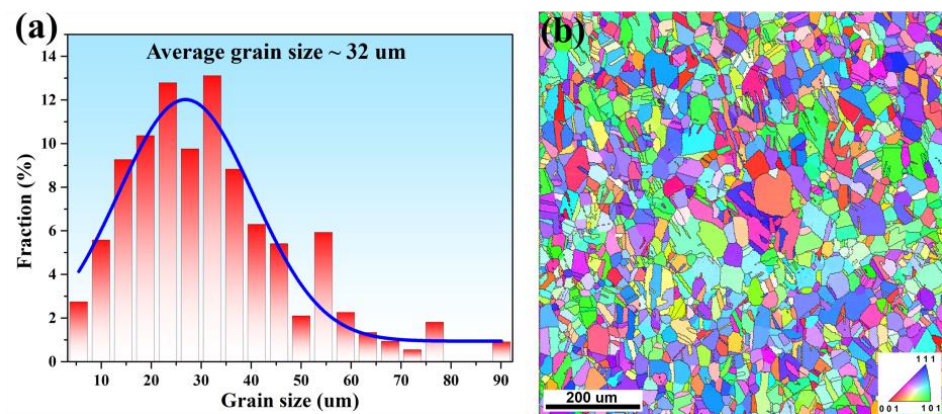
Figure 2. (**a**) Grain size distributions of initial CoCrFeMnNi workpiece; (**b**) a typical EBSD IPF orientation map of the initial workpiece (the inset is the IPF color code).
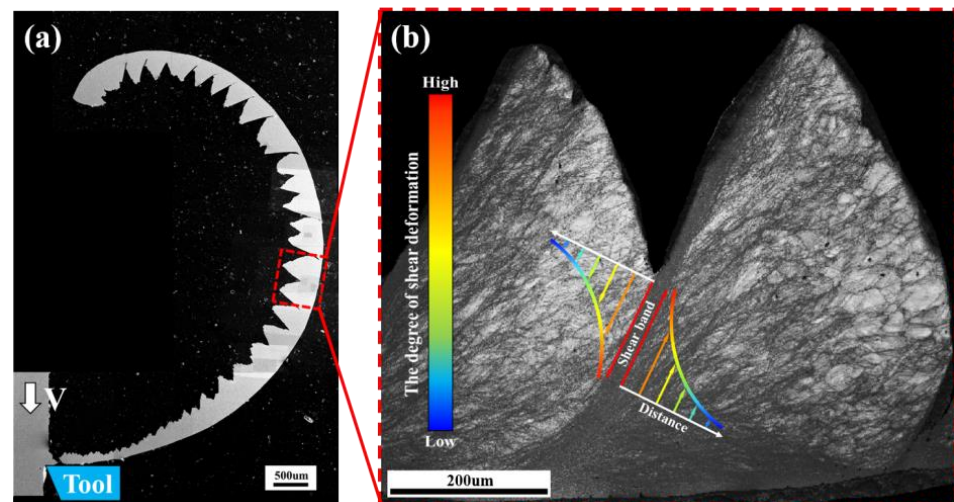

Figure 3. The microstructure of serrated chip formation at cutting speed of 15 m/s: (**a**) the morphology of chip from SEM; (**b**) EBSD image quality (IQ) map of shear band in the serrated chip.

Figure 4 contains the EBSD micrographs of shear localization zone. The shear bands with widths of about 20 μm are distinguished with black dotted lines. In Figure 4a, the microstructure within the shear localization zone mainly consists of partial equiaxed grains and narrow elongated grains. With the shear deformation, the grains on both sides of the shear band were elongated, while the directions were opposite. Figure 4b shows a detailed microstructure outside the shear band (marked with black rectangle in Figure 4a). The grains adjacent to the shear band were severely elongated and partially

fragmented. Meanwhile, the grains far away from shear band were slightly elongated and maintained their original microstructure characteristic. Figure 4c presents a kernel average misorientation (KAM) map investigated outside the shear band. In general, KAM values represent the density of the geometrically necessary dislocation (GND) [36]. According to the color bar, the color changed from blue through yellow to red, indicating an increase in local strain and dislocation density. The black dash line marks the boundary position between shear and matrix. The matrix region outside the shear band is mainly presented in green and yellow, while the shear band is mainly shown in blue, indicating that the dislocation density in the matrix region is higher than that in the shear band. The relatively low dislocation density within the shear band indicates dynamic recrystallization (DRX) in the shear band formation process. DRX can be identified based on the low internal misorientation level resulting from a lower dislocation density as compared to the deformed grains [37]. The grain orientation spread (GOS) is considered to be a successful tool in measuring intragranular orientation gradient [38]. The GOS is calculated by averaging the deviation between the orientation of each point in a given grain and the average orientation of that grain [38–40]. The GOS approach, which is based on the principle that the GOS values of recrystallized grains are lower than those of deformed grains, can be used to determine DRX structures. A threshold value of 2° was chosen for the GOS tolerance to distinguish a recrystallized grain from a deformed one [40,41]. Figure 4d shows a GOS map obtained outside the shear band. As illustrated in Figure 4d, the area outside the shear band consisted mostly of elongated (sub)grains and deformed grains (marked with orange and red colors), together with some small equiaxed grains (expressed by green or blue colors). The shear band region consisted of recrystallized grains with very low dislocation densities.
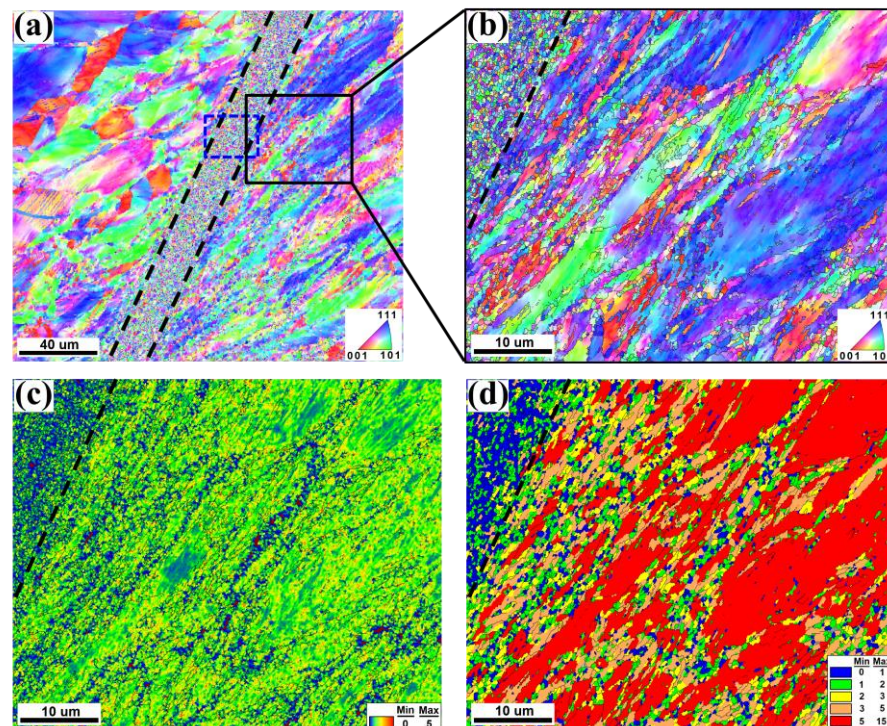
Figure 4. EBSD micrographs of the shear localization zone (step size: 150 nm): (**a**) IPF orientation map; (**b**) IPF orientation map of areas adjacent to the shear band; (**c**) KAM map of areas adjacent to the shear band; (**d**) GOS map of areas adjacent to the shear band.

Figure 5a displays the EBSD micrographs of the shear band (marked with a blue dotted rectangle in Figure 4a) to reveal the microstructure details. As shown in Figure 5a,b, the microstructure within the shear band was mainly composed of many equiaxed ultrafine grains bounded by HAGBs and some elongated large grains. It is generally accepted that

these equiaxed ultrafine grains are the result of grain fragmentation and even dynamic recrystallization during the shear banding process [32,42–45]. Figure 5c shows that the grain size was refined to about 267 nm inside the shear band that broke into ultrafine and nanocrystalline regimes. The misorientation angle distribution reveals that a significant fraction of HAGBs were well developed (Figure 5d), which also indicates the occurrence of dynamic recrystallization. To further understand the dislocation distribution in the shear band, a detailed KAM map superimposed by HAGBs is shown in Figure 5e. High-density dislocations were concentrated in areas close to (sub)grain boundaries, and there was less dislocation in (sub)grain interiors. The low-density dislocations inside the most equiaxed grains clearly indicate that dynamic recrystallization occurred in the shear band. This is also evidenced by the fact that almost all grains were equiaxed recrystallized grains surrounded by well-defined HAGBs, as shown in Figure 5f.
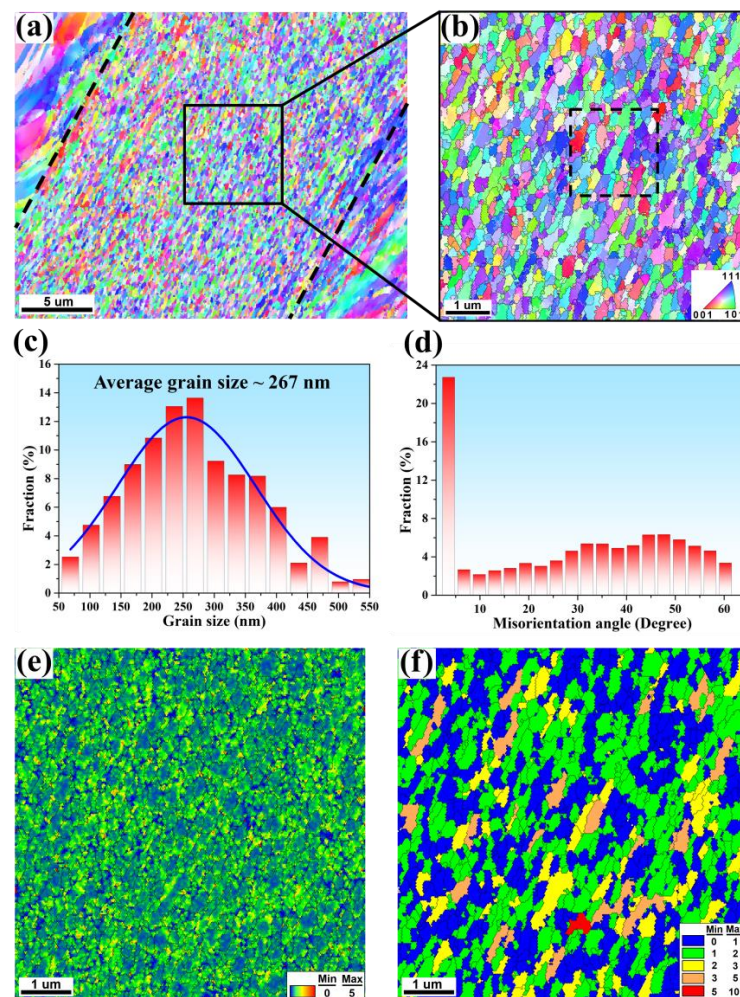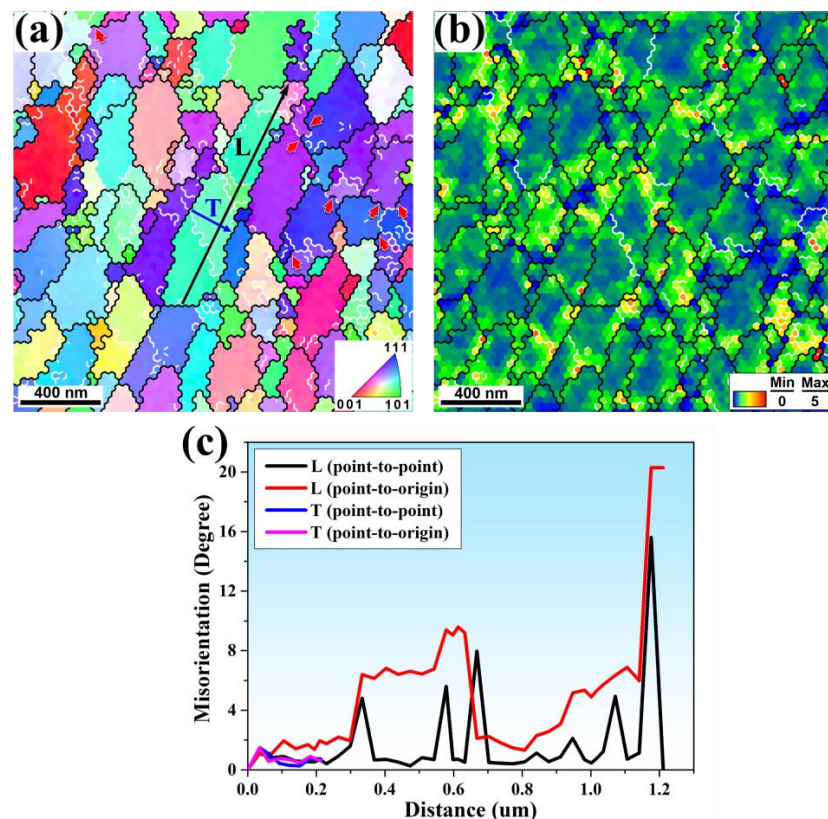

Figure 5. EBSD micrographs of the shear band (step size: 35 nm): (**a**) IPF orientation map; (**b**) IPF orientation map in center of shear band; (**c**) grain size distributions inside shear band; (**d**) grains' misorientation angle distributions inside shear band; (**e**) KAM map superimposed by HAGBs; (**f**) GOS map superimposed by HAGBs.

As mentioned above, in addition to ultrafine equiaxed grains, there were some elongated large grains in the shear zone. Figure 6a gives an enlarged view of the elongated grains (marked with a black dotted rectangle in Figure 5b) inside the shear band. The elongated grain was bounded by HAGBs (black line) and separated by LAGBs (white line), which is a typical microstructure characteristic of subgrains. From Figure 6b, it can be seen that there were relatively high-density dislocations concentrated at LAGBs, implying that LAGBs are formed by the pileup of dislocations. The LAGBs would further transform

into HAGBs with further shear deformation. Actually, some parts of LAGBs, as indicated by red arrows in Figure 6a, evolved into HAGBs. The gradual transformation process is the subgrain rotation nucleation stage in dynamic recrystallization [46,47], which results in a high fraction of HAGBs within the shear band, as shown in Figure 5d. To further understand the grain refinement process in the elongated (sub)grain within the shear band, the micorientation profile within individual elongated (sub)grain was measured. Figure 6c presents the point-to-point and point-to-original misorientation profiles along the path "L" and "T" drawn in an elongated (sub)grain in Figure 6a. Four misorientation jumps below 15° on the point-to-point curve along "L" indicate the existence of four LAGBs, which resulted from the dislocation pileup. There was little misorientation accumulation within these subgrains, which is consistent with the KAM map in Figures 5e and 6b. The point-to-point curve along "T" illustrates the misorientation change below 2°, indicating low local strain along the transverse axis in the elongated grain. These observations elucidate that with further shear deformation, LAGBs would convert gradually into HAGBs, and the elongated grains were broken up into equiaxed ultrafine grains via the fragment of longitudinal axis. Figure 7 illustrates the whole process of the microstructure evolution in the shear band, which is based on the EBSD observations. At the beginning of deformation, the matrix material still retained a large grain size, and the dislocations multiplied rapidly (Figure 7a). As the strain increased, the dislocations rearranged into elongated dislocation cells (Figure 7b). With a further increase in strain, the accumulation and rearrangement of dislocations led to the formation of elongated subgrains (Figure 7c). The elongated dislocation cells subdivided into equiaxed parts to accommodate further strain (Figure 7d). As misorientation increased, fragmentized subgrains rotated, leading to the formation of equiaxed ultrafine grains with HAGBs (Figure 7e). Similar behavior has been observed in the shear band of high-strain-rate deformation [17,48].

Figure 6. Detailed EBSD micrographs of elongated large grain inside the shear band (step size: 35 nm): (**a**) a typical IPF orientation map in the shear band superimposed by LAGBs and HAGBs; (**b**) KAM map superimposed by LAGBs and HAGBs; (**c**) the point-to-point and point-to-original misorientation profile along the path "L" and "T" drawn in an elongated grain in (**a**).
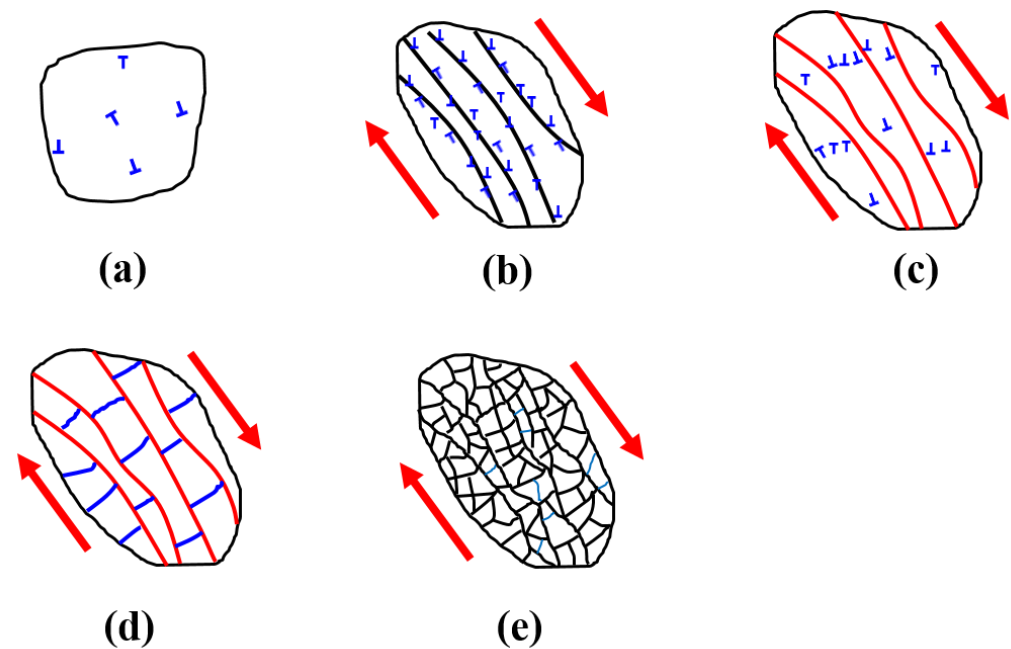
Figure 7. The schematic illustration showing the microstructure evolution in the shear band: (**a**) original equiaxed grain with uniform dislocation distribution; (**b**) formation of dislocation cells; (**c**) formation of elongated subgrains; (**d**) division of elongated sub-grains; (**e**) fragmentized subgrains' rotation and formation of equiaxed ultrafine grains.

4. Conclusions

The chip morphology and microstructure evolution in the shear band, formed during the high-speed cutting of the high-entropy alloy CoCrFeMnNi, were investigated using EBSD. The deformation gradient distribution was found to be heterogeneous in a chip sample, leading to complicated microstructure characteristics and shear band behavior. It was shown that large grains basically kept the original features in the lightly strained areas in the serrated chip. The subsequently elongation and subdivision of the narrow grains were observed in the areas adjacent to the shear band. The microstructure inside the shear band was found to be composed of equiaxed ultrafine grains, with the presence of some elongated ultrafine grains. A microstructure evolution model was proposed, and the related microstructure was attributed to dynamic recrystallization. The present study provides a direct observation inside the shear band for the high-speed cutting of HEA and a fundamental understanding of the serrated chip formation mechanism for high-entropy alloys.

Author Contributions: Conceptualization, M.-Y.S., Y.C. and L.-H.D.; methodology, M.-Y.S., W.-H.Z., Y.C. and L.-H.D.; software, M.-Y.S.; validation, M.-Y.S. and Y.C.; formal analysis, M.-Y.S., W.-H.Z. and Y.-Y.T.; investigation, M.-Y.S. and W.-H.Z.; resources, L.-H.D.; data curation, M.-Y.S.; writing—original draft preparation, M.-Y.S.; writing—review and editing, M.-Y.S., Y.-Y.T., Y.C., H.-Y.W. and L.-H.D.; supervision, L.-H.D.; project administration, L.-H.D.; funding acquisition, Y.-Y.T. and L.-H.D. All authors have read and agreed to the published version of the manuscript.

Data Availability Statement: Available from the corresponding author upon request.

Conflicts of Interest: The authors declare no conflict of interest.

References

1. Flom, D.G.; Komanduri, R.; Lee, M. High-Speed Machining of Metals. *Annul. Rev. Mater. Sci.* **1984**, *14*, 231–278. [CrossRef]
2. Sagapuram, D.; Udupa, A.; Viswanathan, K.; Mann, J.B.; M'Saoubi, R.; Sugihara, T.; Chandrasekar, S. On the Cutting of Metals: A Mechanics Viewpoint. *J. Manuf. Sci. Eng.* **2020**, *142*, 110808. [CrossRef]
3. Shaw, M.C. *Metal Cutting Principles*, 2nd ed.; Oxford University Press: New York, NY, USA, 2005.
4. Ye, G.G.; Jiang, M.Q.; Xue, S.F.; Ma, W.; Dai, L.H. On the instability of chip flow in high-speed machining. *Mech. Mater.* **2018**, *116*, 104–119. [CrossRef]
5. Molinari, A.; Musquar, C.; Sutter, G. Adiabatic shear banding in high speed machining of Ti-6Al-4V: Experiments and modeling. *Int. J. Plast.* **2002**, *18*, 443–459. [CrossRef]
6. Burns, T.J.; Davies, M.A. On repeated adiabatic shear band formation during high-speed machining. *Int. J. Plast.* **2002**, *18*, 487–506. [CrossRef]
7. Huang, J.; Kalaitzidou, K.; Sutherland, J.W.; Aifantis, E.C. Validation of a Predictive Model for Adiabatic Shear Band Formation in Chips Produced via Orthogonal Machining. *J. Mech. Behav. Mater.* **2007**, *18*, 243–264. [CrossRef]
8. Recht, R.F. Catastrophic Thermoplastic Shear. *J. Appl. Mech.* **1964**, *31*, 189–193. [CrossRef]
9. Hou, Z.B.; Komanduri, R. Modeling of thermomechanical shear instability in machining. *Int. J. Mech. Sci.* **1997**, *39*, 1273–1314. [CrossRef]
10. Duan, C.; Wang, M. Some metallurgical aspects of chips formed in high speed machining of high strength low alloy steel. *Scr. Mater.* **2005**, *52*, 1001–1004. [CrossRef]
11. Ye, G.G.; Xue, S.F.; Jiang, M.Q.; Tong, X.H.; Dai, L.H. Modeling periodic adiabatic shear band evolution during high speed machining Ti-6Al-4V alloy. *Int. J. Plast.* **2013**, *40*, 39–55. [CrossRef]
12. Cai, S.L.; Dai, L.H. Suppression of repeated adiabatic shear banding by dynamic large strain extrusion machining. *J. Mech. Phys. Solids* **2014**, *73*, 84–102. [CrossRef]
13. Zeng, F.; Jiang, M.Q.; Dai, L.H. Dilatancy induced ductile-brittle transition of shear band in metallic glasses. *Proc. R. Soc. A-Math. Phys. Eng. Sci.* **2018**, *474*, 20170836. [CrossRef] [PubMed]
14. Bai, Y.L.; Dodd, B. *Adiabatic Shear Localization: Occurrence, Theories, and Applications*; Pergamon Press: Oxford, UK, 1992.
15. Meyers, M.A. *Dynamic Behavior of Materials*; John Wiley & Sons: New York, NY, USA, 1994.
16. Rittel, D.; Landau, P.; Venkert, A. Dynamic recrystallization as a potential cause for adiabatic shear failure. *Phys. Rev. Lett.* **2008**, *101*, 165501. [CrossRef] [PubMed]
17. Yan, N.; Li, Z.; Xu, Y.; Meyers, M.A. Shear localization in metallic materials at high strain rates. *Prog. Mater. Sci.* **2021**, *119*, 100755. [CrossRef]
18. Jiang, M.Q.; Dai, L.H. Formation mechanism of lamellar chips during machining of bulk metallic glass. *Acta Mater.* **2009**, *57*, 2730–2738. [CrossRef]
19. Gludovatz, B.; Hohenwarter, A.; Catoor, D.; Chang, E.H.; George, E.P.; Ritchie, R.O. A fracture-resistant high-entropy alloy for cryogenic applications. *Science* **2014**, *345*, 1153–1158. [CrossRef] [PubMed]
20. Liu, D.; Yu, Q.; Kabra, S.; Jiang, M.; Forna-Kreutzer, P.; Zhang, R.; Payne, M.; Walsh, F.; Gludovatz, B.; Asta, M.; et al. Exceptional fracture toughness of CrCoNi-based medium- and high-entropy alloys at 20 kelvin. *Science* **2022**, *378*, 978–983. [CrossRef]
21. George, E.P.; Raabe, D.; Ritchie, R.O. High-entropy alloys. *Nat. Rev. Mater.* **2019**, *4*, 515–534. [CrossRef]
22. Li, Z.; Pradeep, K.G.; Deng, Y.; Raabe, D.; Tasan, C.C. Metastable high-entropy dual-phase alloys overcome the strength–ductility trade-off. *Nature* **2016**, *534*, 227–230. [CrossRef]
23. Lei, Z.; Liu, X.; Wu, Y.; Wang, H.; Jiang, S.; Wang, S.; Hui, X.; Wu, Y.; Gault, B.; Kontis, P.; et al. Enhanced strength and ductility in a high-entropy alloy via ordered oxygen complexes. *Nature* **2018**, *563*, 546–550. [CrossRef]
24. Pan, Q.; Zhang, L.; Feng, R.; Lu, Q.; An, K.; Chuang, A.C.; Poplawsky, J.D.; Liaw, P.K.; Lu, L. Gradient cell-structured high-entropy alloy with exceptional strength and ductility. *Science* **2021**, *374*, 984–989. [CrossRef]
25. Pu, Z.; Chen, Y.; Dai, L.H. Strong resistance to hydrogen embrittlement of high-entropy alloy. *Mater. Sci. Eng. A* **2018**, *736*, 156–166. [CrossRef]
26. Luo, H.; Sohn, S.S.; Lu, W.; Li, L.; Li, X.; Soundararajan, C.K.; Krieger, W.; Li, Z.; Raabe, D. A strong and ductile medium-entropy alloy resists hydrogen embrittlement and corrosion. *Nat. Commun.* **2020**, *11*, 3081. [CrossRef] [PubMed]
27. Zhang, Z.; Mao, M.M.; Wang, J.; Gludovatz, B.; Zhang, Z.; Mao, S.X.; George, E.P.; Yu, Q.; Ritchie, R.O. Nanoscale origins of the damage tolerance of the high-entropy alloy CrMnFeCoNi. *Nat. Commun.* **2015**, *6*, 10143. [CrossRef] [PubMed]
28. Cai, Z.; Wei, N.; Han, Y.; Si, F.; Mi, L.; Zhang, C.; Liu, X.; Jiang, F.; Wu, T. Effect of Heat Treatment on Microstructure, Tensile Properties and High-Temperature Corrosion Resistance of the FeCrMnNi High Entropy Alloy. *Metals* **2022**, *12*, 1537. [CrossRef]
29. El-Atwani, O.; Li, N.; Li, M.; Devaraj, A.; Baldwin, J.K.S.; Schneider, M.M.; Sobieraj, D.; Wróbel, J.S.; Nguyen-Manh, D.; Maloy, S.A.; et al. Outstanding radiation resistance of tungsten-based high-entropy alloys. *Sci. Adv.* **2019**, *5*, eaav2002. [CrossRef]
30. Liu, X.-F.; Tian, Z.-L.; Zhang, X.-F.; Chen, H.-H.; Liu, T.-W.; Chen, Y.; Wang, Y.-J.; Dai, L.-H. "Self-sharpening" tungsten high-entropy alloy. *Acta Mater.* **2020**, *186*, 257–266. [CrossRef]
31. Chen, J.; Liu, T.-W.; Cao, F.-H.; Wang, H.-Y.; Chen, Y.; Dai, L.-H. Deformation Behavior and Microstructure Evolution of CoCrNi Medium-Entropy Alloy Shaped Charge Liners. *Metals* **2022**, *12*, 811. [CrossRef]
32. Li, Z.; Zhao, S.; Alotaibi, S.M.; Liu, Y.; Wang, B.; Meyers, M.A. Adiabatic shear localization in the CrMnFeCoNi high-entropy alloy. *Acta Mater.* **2018**, *151*, 424–431. [CrossRef]

33. Li, Z.; Zhao, S.; Ritchie, R.O.; Meyers, M.A. Mechanical properties of high-entropy alloys with emphasis on face-centered cubic alloys. *Prog. Mater. Sci.* **2018**, *102*, 296–345. [CrossRef]

34. Tang, Y.; Wang, R.; Xiao, B.; Zhang, Z.; Li, S.; Qiao, J.; Bai, S.; Zhang, Y.; Liaw, P.K. A review on the dynamic-mechanical behaviors of high-entropy alloys. *Prog. Mater. Sci.* **2023**, *135*, 101090. [CrossRef]

35. Wang, Q.; Lu, C.; Ye, G.G.; Dai, L.H. Modelling the tuned criticality in stick-slip friction during metal cutting. *Model. Simul. Mater. Sci. Eng.* **2015**, *23*, 055013. [CrossRef]

36. Kubin, L.P.; Mortensen, A. Geometrically necessary dislocations and strain-gradient plasticity: A few critical issues. *Scr. Mater.* **2003**, *48*, 119–125. [CrossRef]

37. Humphreys, F.J.; Rohrer, G.S.; Rollett, A. *Recrystallization and Related Annealing Phenomena*, 3rd ed.; Elsevier: Oxford, UK, 2017.

38. Mitsche, S.; Poelt, P.; Sommitsch, C. Recrystallization behaviour of the nickel-based alloy 80 A during hot forming. *J. Microsc.* **2007**, *227*, 267–274. [CrossRef] [PubMed]

39. Mirzadeh, H.; Cabrera, J.M.; Najafizadeh, A.; Calvillo, P.R. EBSD study of a hot deformed austenitic stainless steel. *Mater. Sci. Eng. A* **2012**, *538*, 236–245. [CrossRef]

40. Field, D.; Bradford, L.; Nowell, M.; Lillo, T. The role of annealing twins during recrystallization of Cu. *Acta Mater.* **2007**, *55*, 4233–4241. [CrossRef]

41. Cao, Y.; Di, H.; Zhang, J.; Zhang, J.; Ma, T.; Misra, R.D.K. An electron backscattered diffraction study on the dynamic recrystallization behavior of a nickel–chromium alloy (800H) during hot deformation. *Mater. Sci. Eng. A* **2013**, *585*, 71–85. [CrossRef]

42. Grebe, H.A.; Pak, H.-R.; Meyers, M.A. Adiabatic shear localization in titanium and Ti-6 pct Al-4 pct V alloy. *Metall. Trans. A* **1985**, *16*, 761–775. [CrossRef]

43. Meyers, M.A.; Xu, Y.B.; Xue, Q.; Pérez-Prado, M.T.; McNelley, T.R. Microstructural evolution in adiabatic shear localization in stainless steel. *Acta Mater.* **2003**, *51*, 1307–1325. [CrossRef]

44. Li, Z.; Wang, B.; Zhao, S.; Valiev, R.Z.; Vecchio, K.S.; Meyers, M.A. Dynamic deformation and failure of ultrafine-grained titanium. *Acta Mater.* **2017**, *125*, 210–218. [CrossRef]

45. Li, W.; Wang, B.; Huang, X.; Liu, B.; Brechtl, J.; Liaw, P.K. Mechanical behavior and shear band of a powder-metallurgy-fabricated CoCrFeMnNi high-entropy alloy during high strain-rate deformation. *J. Mater. Res. Technol.* **2022**, *21*, 1461–1478. [CrossRef]

46. Meyers, M.A.; Nesterenko, V.F.; LaSalvia, J.C.; Xue, Q. Shear localization in dynamic deformation of materials: Microstructural evolution and self-organization. *Mater. Sci. Eng. A-Struct. Mater. Prop. Microstruct. Process.* **2001**, *317*, 204–225. [CrossRef]

47. Sun, J.L.; Trimby, P.W.; Yan, F.K.; Liao, X.Z.; Tao, N.R.; Wang, J.T. Shear banding in commercial pure titanium deformed by dynamic compression. *Acta Mater.* **2014**, *79*, 47–58. [CrossRef]

48. Murr, L.E.; Trillo, E.A.; Pappu, S.; Kennedy, C. Adiabatic shear bands and examples of their role in severe plastic deformation. *J. Mater. Sci.* **2002**, *37*, 3337–3360. [CrossRef]